

Experimental investigation of ionization front propagating in a 28 GHz gyrotron beam: Observation of plasma structure and spectroscopic measurement of gas temperature

Cite as: J. Appl. Phys. **127**, 063301 (2020); <https://doi.org/10.1063/1.5144157>

Submitted: 28 December 2019 . Accepted: 26 January 2020 . Published Online: 11 February 2020

Kuniyoshi Tabata , Yuki Harada, Yusuke Nakamura , Kimiya Komurasaki , Hiroyuki Koizumi , Tsuyoshi Kariya , and Ryutaro Minami 



View Online



Export Citation



CrossMark

ARTICLES YOU MAY BE INTERESTED IN

[Evaluation of performance of near-field thermophotovoltaic systems based on entropy analysis](#)

Journal of Applied Physics **127**, 063103 (2020); <https://doi.org/10.1063/1.5135729>

[Generation and modulation of terahertz gradient force in the interactions of two-color laser pulses with magnetized plasmas](#)

Journal of Applied Physics **127**, 063302 (2020); <https://doi.org/10.1063/1.5118914>

[Visualizing light trapping within textured silicon solar cells](#)

Journal of Applied Physics **127**, 063104 (2020); <https://doi.org/10.1063/1.5131173>



Your Qubits. Measured.

Meet the next generation of quantum analyzers

- Readout for up to 64 qubits
- Operation at up to 8.5 GHz, mixer-calibration-free
- Signal optimization with minimal latency

Find out more



Experimental investigation of ionization front propagating in a 28 GHz gyrotron beam: Observation of plasma structure and spectroscopic measurement of gas temperature

Cite as: J. Appl. Phys. 127, 063301 (2020); doi: 10.1063/1.5144157

Submitted: 28 December 2019 · Accepted: 26 January 2020 ·

Published Online: 11 February 2020



View Online



Export Citation



CrossMark

Kuniyoshi Tabata,^{1,a)} Yuki Harada,¹ Yusuke Nakamura,² Kimiya Komurasaki,¹ Hiroyuki Koizumi,³ Tsuyoshi Kariya,⁴ and Ryutaro Minami⁴

AFFILIATIONS

¹Department of Aeronautics and Astronautics, The University of Tokyo, 7-3-1 Hongo, Bunkyo-Ku, Tokyo 113-8656, Japan

²Department of Aerospace Engineering, Nagoya University, Furo-Cho, Chikusa-Ku, Nagoya, Aichi 464-8603, Japan

³Department of Advanced Energy, The University of Tokyo, 5-1-5 Kashiwanoha, Kashiwa, Chiba 277-8561, Japan

⁴Plasma Research Center, University of Tsukuba, 1-1-1 Tennodai, Tsukuba, Ibaraki 305-8577, Japan

^{a)}Author to whom correspondence should be addressed: k.tabata@al.t.u-tokyo.ac.jp

ABSTRACT

Atmospheric millimeter-wave discharge was investigated experimentally using a 28 GHz gyrotron. The propagation velocity of an ionization front, plasma structure, and vibrational and rotational temperatures of nitrogen molecules were measured at a beam intensity lower than 1.0 GW/m^2 , which is below the breakdown threshold. Results show that the propagation velocity of an ionization front increased monotonically with beam intensity and decreased with ambient pressure. In addition, four typical plasma structures having different space occupancies were observed. Furthermore, at any beam intensity below 0.5 GW/m^2 , the vibrational temperature was found to be saturated at about 6000 K. The corresponding electron number density is almost equal to the cut-off density. Finally, it was suggested that the propagation velocity depends on the plasma space occupancy.

Published under license by AIP Publishing. <https://doi.org/10.1063/1.5144157>

NOMENCLATURE

| | |
|------------------|---------------------------------------|
| E | Electric field |
| e | Elementary charge |
| f | Millimeter-wave frequency |
| g_N, g_+ | Statistical weights |
| h | Planck's constant |
| k | Wavenumber |
| k_B | Boltzmann's constant |
| m_s | Mass of species s |
| N | Number density of neutral particles |
| n_c | Cut-off density in collisional plasma |
| n_e | Electron number density |
| P_{MMW} | Power of millimeter-wave |
| p | Pressure |
| S | Beam intensity |

| | |
|--|---|
| S_{peak} | Peak intensity of millimeter-wave |
| T_e | Electron temperature |
| $T_{\text{vib}}, T_{\text{rot}}, T_{\text{trans}}$ | Vibrational, rotational and translational temperature |
| U_1 | Propagation velocity of an ionization front |
| V_i | Ionization energy |
| w_0 | Beam radius of millimeter-wave |

Greek

| | |
|-----------------------------|---|
| α | Degree of ionization |
| $\Delta h_{\text{average}}$ | Space-averaged specific enthalpy increase |
| Δh_{local} | Local specific enthalpy increase |
| ϵ_0 | Vacuum permittivity |
| ϵ | Internal energy |
| Θ_{vib} | Vibration characteristic temperature |

ν_m Electron-neutral momentum transfer frequency
 ρ_1 Mass density in front of an ionization front

I. INTRODUCTION

Although many studies have specifically examined atmospheric discharge using direct current or RF waves and microwave waves,¹ few studies have investigated atmospheric discharge using millimeter-waves. Recently, high-power millimeter-wave oscillators (gyrotrons) have been developed,² making atmospheric millimeter-wave discharge possible. Gyrotrons have been developed intensively for heating nuclear fusion plasma. Gyrotrons are used for electron cyclotron resonance heating (ECH) and electron cyclotron current drive (ECCD) phenomena. A gyrotron can generate a high-power millimeter-wave using the cyclotron resonance maser (CRMs) phenomenon. Recently, it has become possible to oscillate multifrequency millimeter-waves, with multimewatt output power.

Atmospheric millimeter-wave discharge may be useful as an ultraviolet light source,^{3,4} for detection of radioactive materials,⁵ for chemical decomposition,⁶ and for beamed energy propulsion.^{7–12} In propulsion applications, millimeter-wave energy is converted efficiently to gas pressure through the atmospheric discharge. First, after a millimeter-wave beam is focused by a parabolic mirror, plasma is ignited. Then, an ionization front propagates with a shock wave toward millimeter-wave beam source. During this process, the air is heated isometrically. A thruster obtains an impulsive thrust force. To estimate the pressure behind plasma, one must ascertain the relation between the beam intensity and propagation velocity, which determines the value of the source term in an equation of conservation of energy. The propagation velocity of the ionization front must be investigated to optimize the propulsion system.

The breakdown threshold is the critical intensity at which the rate is balanced between ionization by collisions between electrons and neutral particles, and electron attachment.¹³ Millimeter-wave discharge is classified according to whether the local millimeter-wave electric field is over or under the critical intensity, respectively, designated as an overcritical or undercritical condition.^{14,15} First, the studies of overcritical millimeter-wave discharge are explained. For the experiments,^{16–22} a 110 GHz millimeter-wave beam is focused. The plasma is ignited at its focal point. Dependence of the critical intensity on ambient pressure was investigated.²⁰ In the experiments, the ignited plasma propagated toward the millimeter-wave source at 10 km/s velocity. Plasma filaments were generated at a quarter-wavelength interval. This phenomenon has been studied by numerical simulation. The results showed that, at the antinode of the standing wave generated by incident beam and reflected beam in front of plasma, the electric field exceeded the critical intensity: a new plasma filament occurred.²³ Furthermore, vibrational and rotational temperatures and the electron number density, which characterize nonthermal plasma in air,²⁴ were investigated using optical emission spectroscopy.^{16,18}

Nevertheless, it remains unclear why an ionization front can propagate toward a millimeter-wave source in undercritical conditions. In 1983, Brodskii generated plasma using an 85 GHz millimeter-wave beam and observed propagation of the ionization

front in a beam with intensity that is 1–2 orders of magnitude lower than the critical intensity.^{25,26} Dependence of the propagation velocity on beam intensity S was changed at $S^* = 0.03 \text{ GW/m}^2$. At $S < S^*$, the dependence is linear. At $S > S^*$, it becomes approximately quadratic. To explain ionization front propagation, which cannot be explained by thermal conduction from bulk plasma to the front, Bogatov *et al.* proposed that the ultraviolet radiation generated a preionization region in front of bulk plasma and that discharge is induced in the region.²⁷ However, this model did not estimate the propagation velocity in the range where the propagation velocity is greater than the speed of sound.

In 2006, Oda *et al.* conducted experiments using a MW-class 170 GHz millimeter-wave at the National Institute for Quantum and Radiological Science and Technology (formerly Japan Atomic Energy Agency).² Reportedly, at $S^* > 0.75 \text{ GW/m}^2$, the ionization front propagates at supersonic speed. Furthermore, a filamentary structure differed from the quarter-wavelength structure was observed.²⁸ Takahashi *et al.* proposed that the Townsend number E/N , which affects the ionization frequency directly, becomes larger because of the low number density of heavy particles in the plasma because of gas heating.²⁹ E and N , respectively, represent the local electric field and number density of neutral particles. However, one difficulty is that the obtained propagation velocity is smaller than the experimental value. Moreover, the numerical model is unable to reproduce a discharge at beam intensity where Oda's experiment was conducted. To construct an accurate model that cannot only reproduce discharge at an undercritical, but which can also explain the propagation velocity more accurately, one must investigate parameters that might affect ionization front propagation in atmospheric millimeter-wave discharge.

This report describes millimeter-wave discharge experiments conducted using a 28 GHz high-power gyrotron at the Plasma Research Center, University of Tsukuba. The first objective is to observe the propagation velocity and plasma structures at different ambient pressures and beam intensities. Plasma structures are thought to be related to the propagation velocity. However, few reports describe the relation between plasma structure and propagation velocity. Therefore, in this study, plasma structures were investigated at different ambient pressures and beam intensities.

The second objective is to measure vibrational and rotational temperatures. According to Simek,³⁰ a fundamental role in air discharges is played by the lowest electronically excited and metastable $A^3\Pi_u^+$ state of N_2 . Except for a very long radiative lifetime (approx. 2 s), the N_2 ($A^3\Pi_u^+$) possesses sufficient energy (approx. 6 eV) to initiate many energy transfer and chemical reactions. Guerra *et al.*³¹ described that the main energy reservoirs in nitrogen molecules are the vibrational levels of the N_2 ($X^1\Sigma_g^+$) state. Therefore, the possibility exists that the increase of vibrational temperature enables an increase not only of the electron temperature but also of the electronic excitation temperature because of energy transportation between the translational mode of electrons and the vibrational mode of heavy particles. Nevertheless, no report of the relevant literature describes a study of vibrational and rotational temperatures in undercritical conditions at which the propagation velocity exceeds the supersonic speed. Therefore, in this study, the vibrational and rotational temperatures of nitrogen molecules were investigated using optical emission spectroscopy.

TABLE I. Characteristics of gyrotron, Plasma Research Center, University of Tsukuba.³²

| | |
|------------------------|------------------|
| Frequency (wavelength) | 28 GHz (10.7 mm) |
| Output power | 570 kW |
| Output duration | 100 ms |
| Beam transverse mode | Gaussian-like |
| Electric efficiency | 40% |

II. EXPERIMENTAL APPARATUS

A. High-power millimeter-wave oscillator: Gyrotron

A gyrotron developed at the Plasma Research Center of the University of Tsukuba oscillates a 28 GHz millimeter-wave. Its maximum power output is 570 kW.³² Its specifications are listed in Table I.

B. Measurement apparatus for propagation velocity and plasma structures

The experimental setup is presented in Fig. 1. A linearly polarized 28 GHz millimeter-wave that has a Gaussian-like profile was transmitted through a corrugated waveguide and was collimated. To ignite plasma at a parabolic mirror easily, two mirrors were used to focus the beam. The incident beam was again focused by a parabolic mirror at the other side of the chamber. Breakdown occurred near the focal point. The chamber walls do not affect the breakdown process because the walls are made of acrylic, which is transparent to millimeter-wave. Furthermore, the difference of the propagation velocity between with and without the chamber at 100 kPa was within the deviation in multiple experiments. To

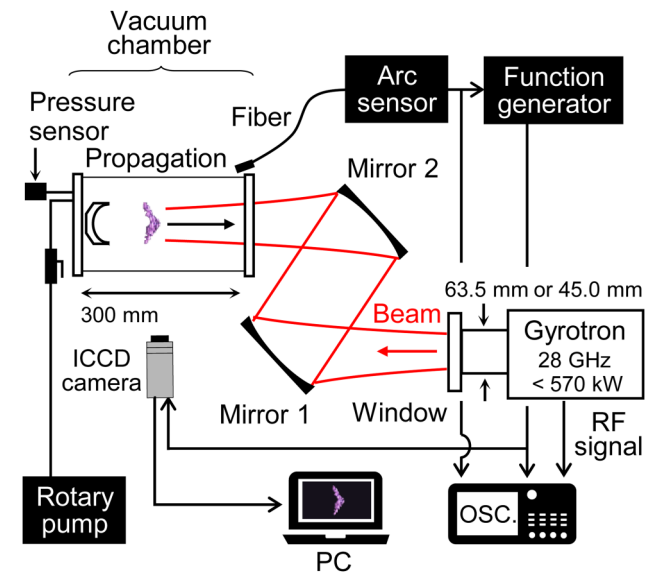


FIG. 1. Schematic of the experimental setup for observing millimeter-wave discharge plasma in a vacuum chamber.

observe plasma in a wider range of peak intensities, corrugated waveguides of two types, with 63.5 mm and 45.0 mm diameter, were used. Furthermore, the beam power was changed from 50 kW to 250 kW. Beam divergence of the millimeter-wave beam was used for a wider range of peak intensities, S_{peak} : 0.05–1.0 GW/m². The following equation defines the peak intensity of the Gaussian-like millimeter-wave:

$$S_{\text{peak}} = \frac{2P_{\text{MMW}}}{\pi w_0^2}. \tag{1}$$

In this equation, P_{MMW} and w_0 , respectively, denote the total power of the millimeter-wave beam and the beam radius. Ambient pressure was changed from 10 kPa to 100 kPa using a rotary pump. A high-speed camera (410 × 360 pixel resolution, Ultra cam; nac Image Technology Inc.) was used to observe the ionization front propagation. The exposure time and frame rate were set, respectively, as 1 μs and as 10–500 kfps. The propagation velocity of an ionization front was calculated by multiplying the propagating distance by the frame rate. Plasma structures were photographed on the E - k plane with colored images, where the incident beam direction vector is denoted by k , and where the electric field vector is denoted by E . An arc sensor was used for the shutter trigger of the camera.

C. Measurement apparatus for optical emission spectroscopy

Optical emission spectroscopy, which does not perturb electromagnetic fields, was applied to measure neutral particle temperatures. The experimental setup is shown in Fig. 2. Two convex lenses were used to focus the light emitted from the plasma onto an optical fiber and the irradiation was collected to a

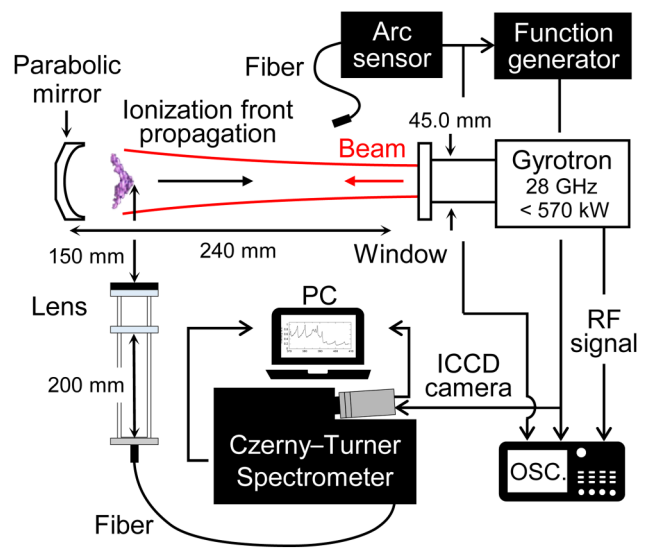


FIG. 2. Simplified schematic of the experimental setup for conducting optical emission spectroscopy in air.

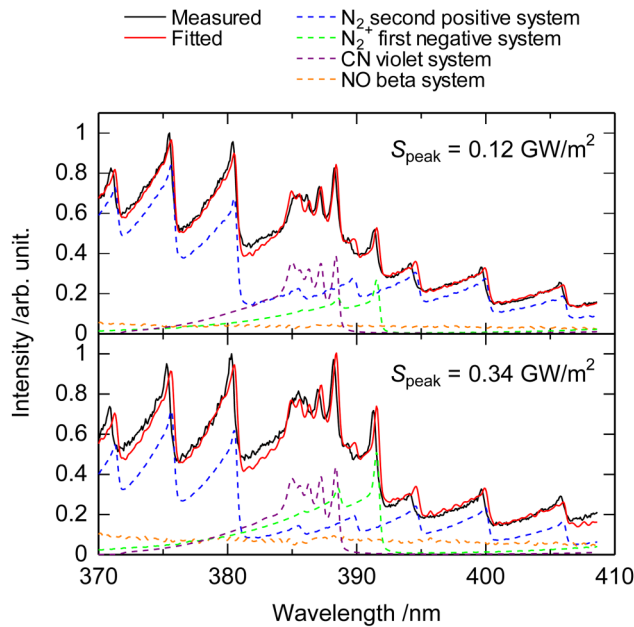


FIG. 3. Examples of fitted emission spectra in the range of 370–410 nm at peak intensities of 0.12 GW/m² and 0.34 GW/m².

Czerny–Turner spectrometer (MS3504i; SOL Instruments Ltd.) with an ICCD camera (iStar sCMOS, 2560 pixel resolution, element size: 6.5 μm; Andor Technology). The reverse dispersion is 2.37 nm/mm. The exposure time and slit width were set, respectively, as 5 ms and 100 μm. The corresponding Δλ is 0.237 nm. The distance between the focal point and waveguide was changed to change peak intensity from 0.067 GW/m² to 0.46 GW/m². In each condition, the emission spectra were measured five times.

Vibrational and rotational temperatures of nitrogen molecules were deduced using measured spectra of second positive systems, which are emitted as transitions from an electronic state C ³Π_u to an electronic state B ³Π_g. The second positive system is often used for measuring vibrational and rotational temperatures because of its strong intensity and simple transition scheme.^{18,33} These transitions appear in the ultraviolet region: 280–400 nm. For this study, the light emission spectrum from 370 nm to 410 nm was measured. A typical emission spectrum is presented in Fig. 3. For measuring vibrational and rotational temperatures from the obtained spectrum, a fitting code was developed using theoretical schemes.^{33–35}

TABLE II. Band systems of molecules considered for theoretical calculation.

| Species | System name | Wavelengths (nm) | Energy level transition |
|-----------------------------|------------------------|------------------|---|
| N ₂ | Second positive system | 280–400 | C ³ Π _u → B ³ Π _g |
| N ₂ ⁺ | First negative system | 320–500 | B ² Σ _u ⁺ → X ² Σ _g ⁺ |
| CN | Violet system | 320–500 | B ² Σ ⁺ → X ² Σ ⁺ |
| NO | Beta system | 200–500 | B ² Π _r → X ² Π _r |

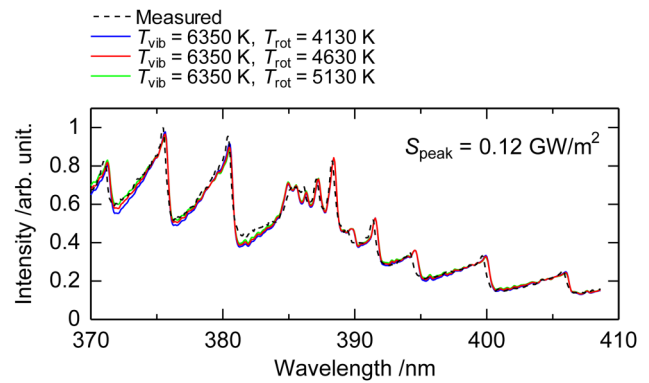


FIG. 4. Examples of fitted emission spectra in the range of 370–410 nm at 0.12 GW/m² peak intensity. The rotational temperature was changed by ±500 K.

As the figure shows, emissions from N₂ I and N₂ II were observed in this region along with those from CN and NO. Therefore, the obtained spectra were fitted using theoretical calculation methods of those emissions. In this calculation, the fitting parameters were each molecule’s vibrational and rotational temperatures and intensity ratios. Here, all the vibrational energy states and rotational energy states were assumed in a Boltzmann equilibrium. Table II presents band systems considered for theoretical calculation when the spectra were fitted. After least-squares fitting, the error was evaluated. Results showed that the measured spectrum was at least within ±500 K, which is shown in the figure as its error. The calculated spectrum when the rotational temperature was changed ±500 K from the deduced one was compared with measured one, as presented in Fig. 4.

Plasma structures of black and white images were also observed in the experimental setup of Fig. 2 using the high-speed framing camera with GaAs CMOS, iStar sCMOS (2560 × 2100 pixel resolution; Andor Technology) to observe plasma structures with higher resolution. The exposure time was set to 1 μs. Figure 5 shows the beam intensity distribution and divergence with an ionization front, which was taken by the iStar sCMOS.

III. RESULTS AND DISCUSSION

A. Plasma structures and ionization front propagation velocity

1. Plasma structures

Observed filamentary plasma images are shown in Fig. 6. Structures (a) and (c) were photographed using an ultracam camera using the setup shown in Fig. 1, whereas (b) and (d) were taken by an iStar sCMOS camera in the setup presented in Fig. 2. Four structures with different plasma space occupancies were observed. Here, the plasma space occupancy is defined as the volume ratio of the plasma to the surrounding air. The structural change of millimeter-wave discharge plasma is mapped in Fig. 7 for different atmospheric pressures and peak intensities. Regions with different background colors indicate different plasma structures, and (a)–(d) in Fig. 7 correspond to the four plasma

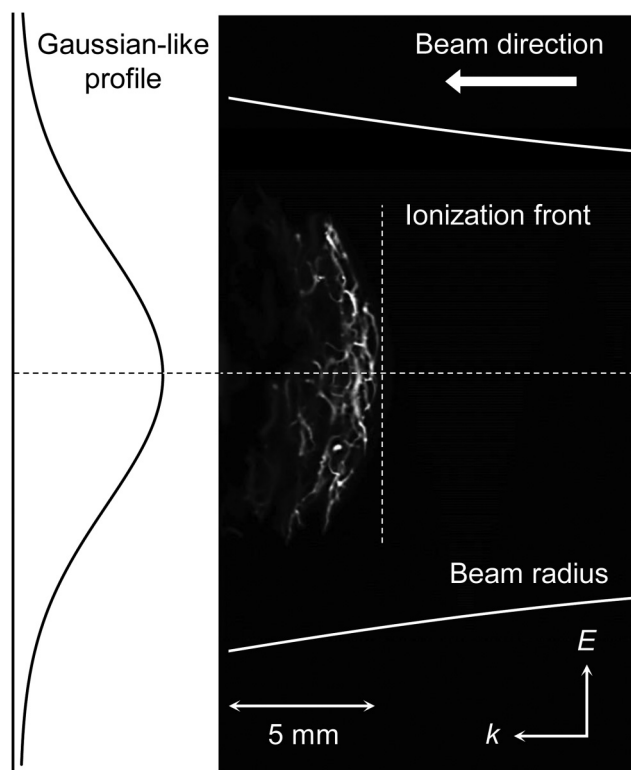


FIG. 5. The right-hand panel depicts an example of an ionization front taken by iStar sCMOS. The left-hand panel shows the beam intensity distribution and divergence.

structures presented in Fig. 6. The boundary lines between the regions are not measured but rather approximated. Structure (a) is designated as the quarter-wavelength structure, which appears at near-critical intensity as already observed for 110 GHz millimeter-wave discharge.²⁰ Structure (b) was observed in undercritical intensity. It looks closely similar to that found in atmospheric microwave discharge.¹ Khodataev reported that the electric field concentration and gas expansion in front of a thin plasma increase the Townsend number E/N and that discharge formation can occur in fields with intensity lower than the critical intensity.¹ When the ambient pressure and S_{peak} are decreased, no discrete structure was observed as presented in (c). Structure (d) is that by which branched plasmoids are spread diffusively toward a millimeter-wave source as it was observed already in 170 GHz millimeter-wave discharge.²⁸ When a flat-topped beam profile was used, the branched plasmoids propagated parallel to the incident beam direction.³⁷ The phenomenon was reproduced numerically.³⁸

2. Ionization front propagation velocity

Figure 8 portrays the dependence on peak intensity of the propagation velocity of millimeter-wave discharge plasma at different ambient pressures. The velocity of an ionization front toward a

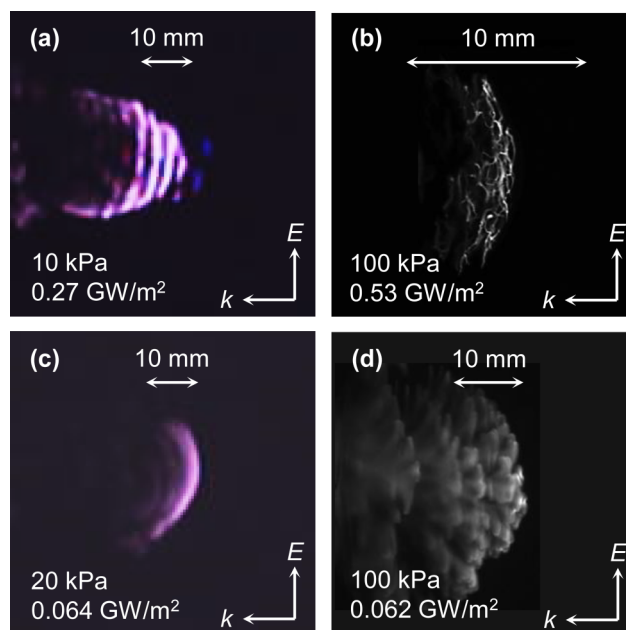


FIG. 6. Characteristic structures observed at various peak intensities and atmospheric pressures. (a) $\lambda/4$ structure; (b) complex structure as observed in microwave discharges; (c) diffusive (no discrete structure); and (d) branched plasmoids spread diffusively.

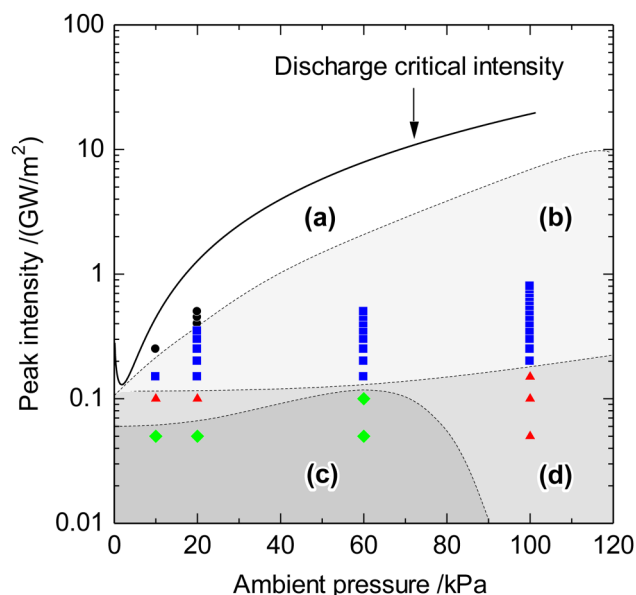


FIG. 7. Characteristic structures observed at various atmospheric pressures and peak intensities. \circ $\lambda/4$ structure; \diamond diffusive (no discrete structure); \triangle branched plasmoids spread diffusively; \square complex structure as observed in microwave discharges. The solid line is a critical intensity deduced by Taylor (24.1 GHz), which is presented as a reference.

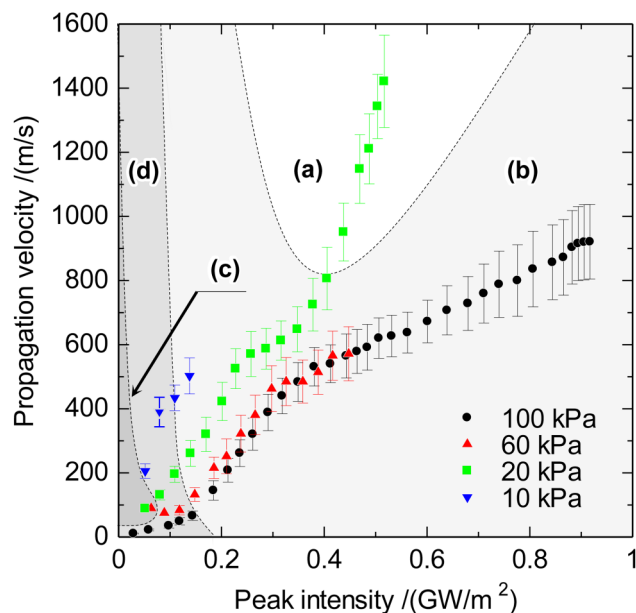


FIG. 8. Dependence of propagating velocity on peak intensity for various ambient pressures. (a) $\lambda/4$ structure; (b) complex structure as observed in microwave discharges; (c) diffusive (no discrete structure); and (d) branched plasmoids spread diffusively.

beam source gets higher and lower because of filament extensions in the radial direction.^{1,19} The error bar in Fig. 8 represents the range between its maximum and minimum velocities. Regions with different background colors indicate different plasma structures and (a)–(d) in Fig. 8 correspond to the four plasma structures presented in Fig. 6. The propagation velocity increased monotonically with S_{peak} . In addition, the lower the ambient pressure was, the higher the propagation velocity became. These characteristics were the same as results obtained from experiments using 170 GHz millimeter-waves.²⁸ Furthermore, the propagation velocity trend changed at a point where the plasma structure was changed.

Although S_{peak} , where the propagation velocity becomes supersonic at 100 kPa, is 0.75 GW/m^2 in the case of 170 GHz,²⁸ it was 0.27 GW/m^2 for the case of 28 GHz. Furthermore, it was reported that the propagation velocities at 134, 170, and 203 GHz exhibit the same tendency.³⁶ However, the tendency of propagation velocity on S_{peak} in 28 GHz was found to differ from the trend. The structural change of plasma might cause these differences. In the case of 170 GHz, the plasma structure did not change at any beam intensities. By contrast, Fig. 8 suggests that the trend of propagation velocity in 28 GHz changed at a point where the plasma structure changed from (d) to (b). This result implies that structural change causes a difference of the energy concentration degree in space, resulting in the change of the tendency of propagation velocity for S_{peak} . It is thought that in the structure (b), a strong standing wave was generated because plasma density reached cut-off density. This phenomenon has to do with the change of the propagation velocity.

B. Vibrational and rotational temperatures of nitrogen molecules

1. Measured temperatures

Figure 9 shows the measured vibrational and rotational temperatures of nitrogen molecules in the region where the plasma luminance is the strongest. No marked change was observed in the vibrational temperature with the change of S_{peak} , in which vibrational temperature was almost 6000 K. The errors in Fig. 9 show $\pm 500 \text{ K}$ as explained in Sec. II C. On the other hand, the rotational temperature decreased from 5500 K to 3000 K for $0.067\text{--}0.46 \text{ GW/m}^2$. This decrease might occur because the propagation velocity is sufficiently low to cause energy relaxation from a vibrational mode to translational and rotational modes. The deduced vibrational temperature and rotational temperature were higher than the earlier experimentally obtained results¹⁸ in overcritical conditions, even though S_{peak} used in this experiment was much lower than the experiment.¹⁸

2. Estimated electron number density

The electron number density in the bulk plasma region was estimated assuming that plasma was in local thermodynamic equilibrium (LTE). The assumption is supported by the fact that the obtained spectra were well fitted to Boltzmann distribution for vibrational and rotational energy levels. The electron number density calculated using Saha's equation shown in Eq. (2) is

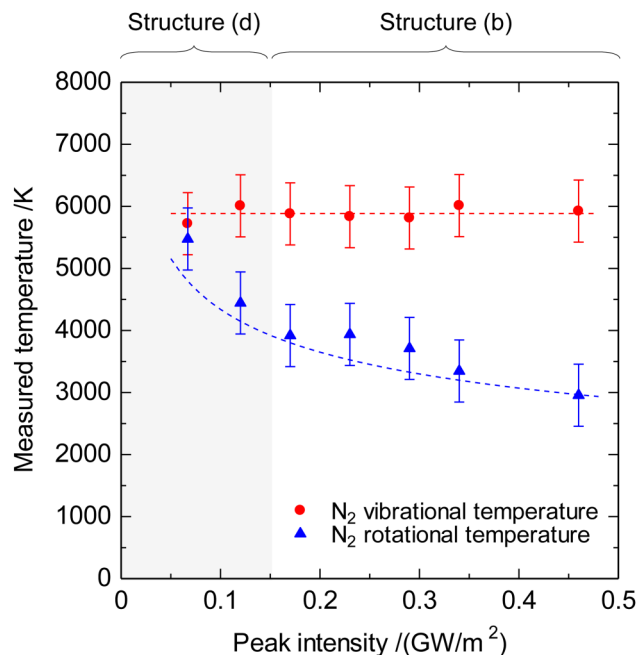


FIG. 9. Deduced vibrational and rotational temperatures of nitrogen molecules at 100 kPa. The curves represent fitting curves.

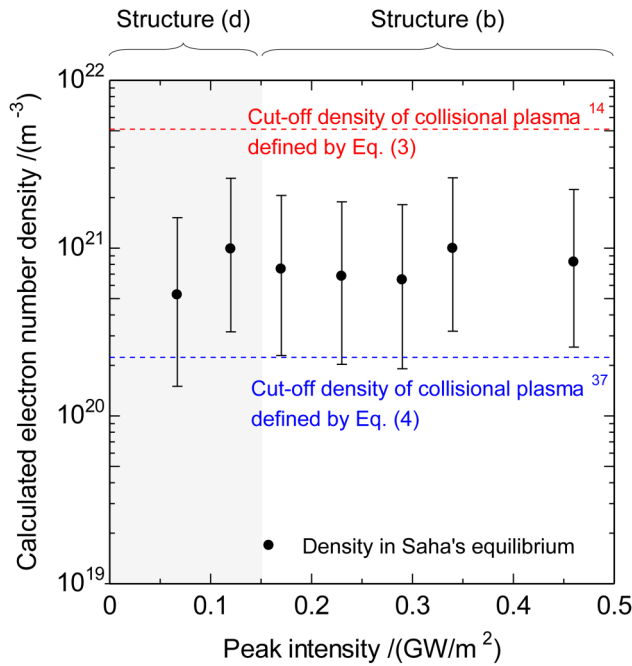


FIG. 10. Local electron number density calculated using Saha's equation and the cut-off electron number density in collisional plasma.

presented in Fig. 10,

$$\frac{n_e^2}{N} = \frac{2g_+}{g_N} \frac{2\pi m_e k_B T_e}{h^2} \exp\left(-\frac{eV_i}{k_B T_e}\right). \quad (2)$$

Here, the ambient air is regarded as consisting of 21% oxygen molecules and 78% nitrogen molecules. The neutral particle density and gas temperature are assumed, respectively, as $2.46 \times 10^{25} \text{ m}^{-3}$ and a rotational temperature. These assumptions mean that neutral particles are heated isometrically. Even in nonthermal plasmas, translational and rotational temperatures are usually regarded as equal because of their short energy relaxation.²⁴ The error of the calculated electron number density corresponds to the error of the deduced vibrational temperatures.

The cut-off electron number density n_c in collisional plasma is written as Eq. (3)¹⁶ or Eq. (4):³⁹

$$n_c = \frac{m_e \epsilon_0}{e^2} (\omega^2 + \nu_m^2), \quad (3)$$

$$n_c = \frac{m_e \epsilon_0}{e^2} \omega \nu_m. \quad (4)$$

Here, $\omega = 2\pi f$ and ν_m , respectively, denote the angular frequency of the millimeter-wave and the electron-neutral particle collision frequency. The cut-off densities are presented in Fig. 10.

These results show that the vibrational temperature was increased to the temperature at which the electron number density

approximately equals the cut-off density. According to an earlier report of the relevant literature,¹⁶ the maximum electron number density is almost equal to the cut-off density defined in Eq. (3). The 28 GHz millimeter-wave discharge experiments results are consistent with the numerical calculation. The electron number density is almost constant at cut-off density in collisional plasma because the reflection by plasma is increased as the value increases over the cut-off value, resulting in the formation of a new filament ahead of the plasma. In experiments using a 110 GHz millimeter-wave with intensity near the critical intensity, the vibrational temperature is not so high as that value.¹⁸ In 110 GHz experimental conditions, the possibility exists that the electron temperature and vibrational temperature are not in equilibrium because the propagation velocity is much higher than that presented in this paper.

C. Energy balance and plasma space occupancy

The ionization front propagation velocity of millimeter-wave discharge is widely known to be higher than that of laser discharge.³⁸ One hypothesis is that the nonuniform plasma shown in Fig. 6 makes the velocity higher because of energy concentration in the local area. Therefore, the plasma space occupancy was investigated to clarify the relation between the propagation velocity and plasma structure. The plasma space occupancy is calculable by the ratio of space-averaged specific enthalpy increase (J/kg) to that in local plasma. In the case where isometric heating can be presumed, the ratio calculated using enthalpy increase per unit mass (specific enthalpy increase) gives plasma space occupancy, which is the volume ratio of the plasma to the surrounding air.

The space-averaged heating rate, which is the specific enthalpy increase, is expressed as Eq. (5),

$$\Delta h_{\text{average}} = \frac{S_{\text{peak}}}{\rho_1 \cdot U_1}. \quad (5)$$

Here, ρ_1 and U_1 , respectively, represent the mass density in front of an ionization front and the ionization front propagation velocity. Here, the nonuniform heating shown in Fig. 6 has not been considered. Equation (5) gives the specific enthalpy increase when an ionization front homogeneously propagates at the speed of U_1 .

The specific enthalpy increase in local plasma was calculated using measured vibrational and rotational temperatures. Here, it was assumed that the particles in plasma regions are heated isometrically. Part of the millimeter-wave energy is consumed for electrons' kinetic energy and ionization energy. Furthermore, the millimeter-wave energy is consumed as the electronic excitation energy, vibrational energy, rotational energy, and translational energy of heavy particles. For this study, it is assumed that the air consists of 21% oxygen molecules and 78% nitrogen molecules. Presuming that local thermodynamic equilibrium (LTE) condition is satisfied, the ionization degree can be deduced using Saha's equation (2). The vibrational energy was calculated using the formula presented in an earlier report.⁴⁰ Rotational and translational energy were followed by the law of equipartition of energy, giving a degree of freedom of 2 for rotational and 3 for translational. Here, translational and rotational temperatures are assumed to be equal because of the reason explained in Sec. III B. Following these assumptions,

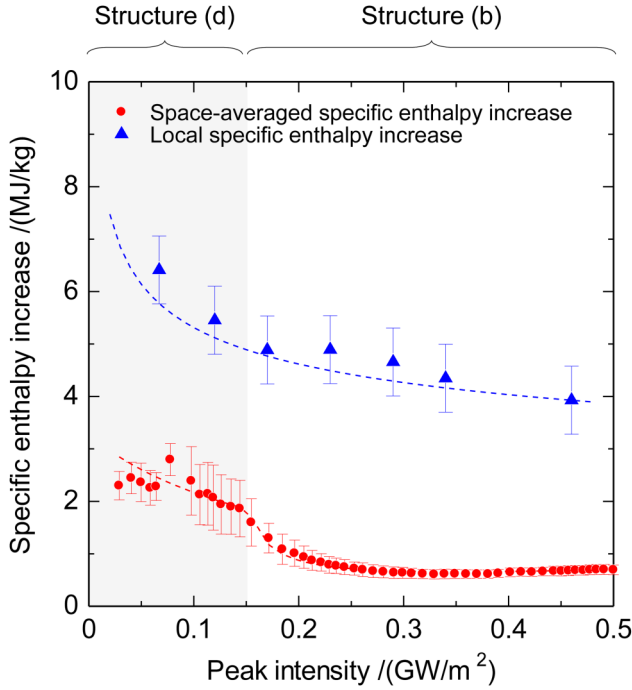


FIG. 11. Local and space-averaged specific enthalpy increase at 100 kPa. The curves represent fitting curves.

the local specific enthalpy increases Δh are expressed in Eq. (6),

$$\Delta h_{\text{local}} = h_{\text{after}} - h_{\text{before}}, \quad (6)$$

$$h = \sum_s \left[\varepsilon + \left(\frac{p}{\rho} \right)_s \right].$$

Here, h_{after} and h_{before} , respectively, stand for the specific enthalpy after the millimeter-wave pulse and before the pulse. Also, s represents the species such as oxygen molecules and nitrogen molecules. ε denotes the specific internal energy calculated using the Eqs. (7)–(11). Each energy is the ionization energy and electrons' kinetic energy, electronic excitation energy, vibrational energy, rotational energy, and translational energy, respectively:

$$\varepsilon_1 = \frac{1}{m_s} \cdot \left(\frac{3}{2} k_B T_e + V_i \right) \cdot \alpha, \quad (7)$$

$$\varepsilon_2 = \frac{1}{m_s} \cdot \frac{\sum_i \varepsilon_{\text{ex},i} \exp(-\varepsilon_{\text{ex},i}/k_B T_e)}{\sum_i \exp(-\varepsilon_{\text{ex},i}/k_B T_e)}, \quad (8)$$

$$\varepsilon_3 = \frac{1}{m_s} \cdot \frac{k_B \Theta_{\text{vib}}}{\exp(\Theta_{\text{vib}}/T_{\text{vib}}) - 1}, \quad (9)$$

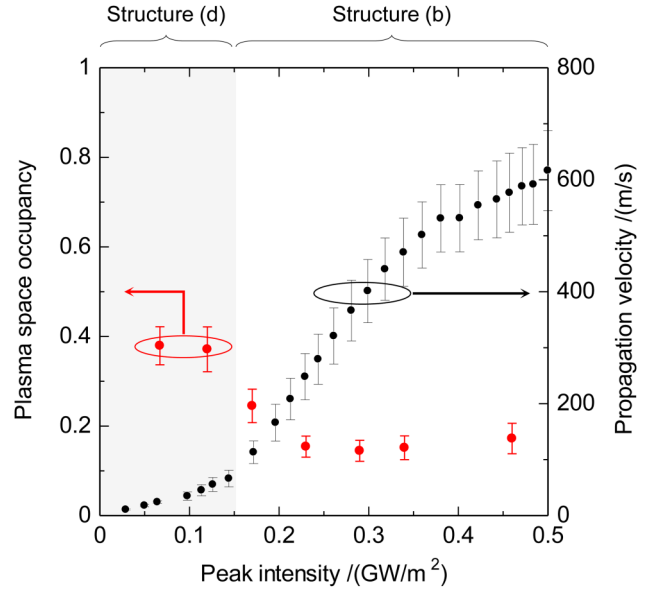


FIG. 12. Calculated plasma space occupancy with measured propagation velocity. Plasma space occupancy was decreased at about 0.15 GW/m^2 , where the propagation velocity was also changed.

$$\varepsilon_4 = \frac{1}{m_s} \cdot k_B T_{\text{rot}}, \quad (10)$$

$$\varepsilon_5 = \frac{1}{m_s} \cdot \frac{3}{2} k_B T_{\text{trans}}. \quad (11)$$

The specific enthalpy increases obtained using Eqs. (5) and (6) are shown in Fig. 11. The local specific enthalpy increases are larger than the space-averaged one because plasma was generated nonuniformly and because heavy particles are heated in the local region. The difference between those values became larger as the beam intensity increased. The calculated plasma space occupancy is shown in Fig. 12. Results confirmed that the plasma space occupancy decreased by half when the plasma structure changed. That change is consistent with the results presented in Figs. 6 and 7. Furthermore, it is readily apparent that the propagation velocity increased with the change of plasma space occupancy. These results indicate that the propagation velocity depends strongly on the plasma space occupancy.

IV. CONCLUSION

Atmospheric millimeter-wave discharge experiments with a peak intensity range below $1.0 \text{ GW}/\text{m}^2$ were conducted using a 28 GHz gyrotron. High-speed photography with $1 \mu\text{s}$ exposure time enabled observation of ionization front propagation. Consequently, the ionization front propagation velocity increased monotonically with an increase of beam intensity and decrease of ambient pressure.

Furthermore, four plasma structures were observed by changing ambient pressure and beam intensity.

Optical emission spectroscopy revealed that the vibrational temperature was saturated at about 6000 K at a peak intensity of 0.062–0.47 GW/m² at 100 kPa. The electron number density was found for cut-off density in collisional plasma, which is consistent with earlier calculated and experimentally obtained results.

Plasma space occupancy was calculated by comparing space-averaged and local specific enthalpy increases. The results revealed that the propagation velocity depends on the plasma space occupancy.

ACKNOWLEDGMENTS

This work was supported by the JSPS KAKENHI under Grant No. JP15H05770.

REFERENCES

- ¹K. V. Khodataev, *J. Propul. Power* **24**(5), 962–972 (2008).
- ²M. K. A. Thumm, G. G. Denisov, K. Sakamoto, and M. Q. Tran, *Nucl. Fusion* **59**, 073001 (2019).
- ³A. V. Sidorov, S. V. Golubev, S. V. Razin, A. P. Veselov, A. V. Vodopyanov, A. P. Fokin, A. G. Luchinin, and M. Y. Glyavin, *J. Phys. D Appl. Phys.* **51**, 464002 (2018).
- ⁴M. Y. Glyavin, S. V. Golubev, I. V. Izotov, A. G. Litvak, A. G. Luchinin, S. V. Razin, A. V. Sidorov, V. A. Skalyga, and A. V. Vodopyanov, *Appl. Phys. Lett.* **105**, 174101 (2014).
- ⁵V. L. Granatstein and G. S. Nusinovich, *J. Appl. Phys.* **108**, 063304 (2010).
- ⁶S. Sintsov, A. Vodopyanov, and D. Mansfeld, *AIP Adv.* **9**, 105009 (2019).
- ⁷K. Komurasaki and K. Tabata, *Int. J. Aerospace Eng.* **2018**, 9247429 (2018).
- ⁸M. Fukunari, K. Komurasaki, Y. Nakamura, Y. Oda, and K. Sakamoto, *J. Energy Power Eng.* **11**, 363–371 (2017).
- ⁹M. Fukunari, A. Arnault, T. Yamaguchi, and K. Komurasaki, *Appl. Opt.* **53**, 31 (2014).
- ¹⁰Y. Oda, T. Shibata, K. Komurasaki, K. Takahashi, A. Kasugai, and K. Sakamoto, *J. Propul. Power* **25**(1), 118–122 (2009).
- ¹¹T. Nakagawa, Y. Mihara, K. Komurasaki, K. Takahashi, K. Sakamoto, and T. Imai, *J. Spacecraft Rockets* **41**(1), 151–153 (2004).
- ¹²T. Yamaguchi, R. Komatsu, M. Fukunari, K. Komurasaki, Y. Oda, K. Kajiwara, K. Takahashi, and K. Sakamoto, *AIP Conf. Proc.* **1402**, 478 (2011).
- ¹³W. C. Taylor, W. E. Scharfman, and T. Morita, *Advances in Microwaves* (Academic, New York, 1971), Vol. 7.
- ¹⁴I. I. Esakov, L. P. Grachev, K. V. Khodataev, and D. M. Van Wie, in *32nd AIAA Plasma Dynamics and Lasers Conference and Fourth Weekly Ionized Gas Workshop*, Anaheim, CA (AIAA, 2001), pp. 2001–2939.
- ¹⁵M. Takahashi and K. Komurasaki, *Adv. Phys. X* **3**(1), 113–144 (2018).
- ¹⁶S. C. Schaub, J. S. Hummelt, W. C. Guss, M. A. Shapiro, and R. J. Temkin, *Phys. Plasmas* **23**, 083512 (2016).
- ¹⁷A. M. Cook, J. S. Hummelt, M. A. Shapiro, and R. J. Temkin, *Phys. Plasmas* **20**, 043507 (2013).
- ¹⁸J. S. Hummelt, M. A. Shapiro, and R. J. Temkin, *Phys. Plasmas* **19**, 123509 (2012).
- ¹⁹A. M. Cook, J. S. Hummelt, M. A. Shapiro, and R. J. Temkin, *Phys. Plasmas* **18**, 100704 (2011).
- ²⁰A. Cook, M. Shapiro, and R. J. Temkin, *Appl. Phys. Lett.* **97**, 011504 (2010).
- ²¹Y. Hidaka, E. M. Choi, I. Mastovsky, M. A. Shapiro, J. R. Sirigiri, R. J. Temkin, G. F. Edmiston, A. A. Neuber, and Y. Oda, *Phys. Plasmas* **16**, 055702 (2009).
- ²²Y. Hidaka, E. M. Choi, I. Mastovsky, M. A. Shapiro, J. R. Sirigiri, and R. J. Temkin, *Phys. Rev. Lett.* **100**, 035003 (2008).
- ²³E. Arcese, F. Rogier, and J. P. Bouef, *Phys. Plasmas* **24**, 113517 (2017).
- ²⁴D. Staack, B. Farouk, A. F. Gutsol, and A. A. Fridman, *Plasma Sources Sci. Technol.* **15**, 818–827 (2006).
- ²⁵Yu. Ya. Brodskii, I. P. Venediktov, S. V. Colubev, V. G. Zorin, and I. A. Kossyi, *Sov. Tech. Phys. Lett.* **10**(2), 77–79 (1984).
- ²⁶A. L. Vikharev, V. B. Gil'denburg, S. V. Golubev, B. G. Eremin, O. A. Ivanov, A. G. Litvak, A. N. Stepanov, and A. D. Yunakovskii, *Sov. Phys. JETP* **67**(4), 724–728 (1988).
- ²⁷N. A. Bogatov, S. V. Golubev, and V. G. Zorin, *Sov. Tech. Phys. Lett.* **9**(7), 382–383 (1983).
- ²⁸Y. Oda, K. Komurasaki, K. Takahashi, A. Kasugai, and K. Sakamoto, *J. Appl. Phys.* **10**, 113307 (2006).
- ²⁹M. Takahashi, Y. Kageyama, and N. Ohnishi, *AIP Adv.* **7**, 055206 (2017).
- ³⁰M. Simek, *Plasma Sources Sci. Technol.* **12**, 421–431 (2003).
- ³¹V. Guerra, P. A. Sa, and J. Loureiro, *J. Phys. D Appl. Phys.* **34**, 1745–1755 (2001).
- ³²T. Kariya, Y. Mitsunaka, T. Imai, T. Saito, Y. Tatematsu, K. Sakamoto, R. Minami, O. Watanabe, T. Numakura, and Y. Endo, *Trans. Fusion Sci. Technol.* **51**(2T), 397–399 (2007).
- ³³H. Akatsuka, in *Chemical Kinetics*, edited by V. Patel (InTech, 2012), ISBN: 978-953-51-0132-1.
- ³⁴F. R. Gilmore, R. R. Laher, and P. J. Espy, *J. Phys. Chem. Ref. Data* **21**(5), 1005–1107 (1992).
- ³⁵D. M. Phillips, *J. Phys. D Appl. Phys.* **8**, 507–521 (1975).
- ³⁶Y. Oda, M. Takahashi, K. Tabata, N. Ohnishi, and K. Komurasaki, IRMMW-THz 2018, Fr-A2-R2-6, Nagoya, Japan, September 2018.
- ³⁷T. Yamaguchi, M. Fukunari, Y. Nakamura, Y. Oda, K. Sakamoto, and K. Komurasaki, *Front. Appl. Plasma Technol.* **9**(2), 79–80 (2016).
- ³⁸Y. Nakamura, K. Komurasaki, M. Fukunari, and H. Koizumi, *J. Appl. Phys.* **124**, 033303 (2018).
- ³⁹W. Woo and J. S. DeGroot, *Phys. Fluids* **27**(2), 475–487 (1984).
- ⁴⁰C. Park, *Nonequilibrium Hypersonic Aerothermodynamics* (Wiley Interscience, 1990).